nature portfolio

https://doi.org/10.1038/s41586-025-09694-5

## Supplementary information

# Evidence for improved DNA repair in the long-lived bowhead whale

In the format provided by the authors and unedited

# Supplementary Information

## Contents

**Supplementary Table 1 |** Lists statistical values corresponding to Extended Data Figure 10c.

**Supplementary Table 2 |** Detailed descriptions and catalog numbers for antibodies, kits, and chemicals used in this study, as well as the sequences of siRNAs and primers.

**Supplementary Figure 1 |** Uncropped gels and Western blots from Main and Extended Data Figures.

**Supplementary Figure 2 |** Synthego ICE analysis of Sanger sequencing data from TP53-edited clones.

**Supplementary Figure 3 |** Synthego ICE analysis and TOPO sequencing of RB1-edited clones.

**Supplementary Figure 4 |** Mutational spectra for all sampled groups in the study.

**Supplementary Figure 5 |** Alignment of PTEN target sequences used in cross-species DSB repair fidelity assays.

**Supplementary Figure 6 |** Transfection efficiency of CRISPR RNPs labeled with ATTO 550.

**Supplementary Figure 7 |** Gating strategy for flow cytometry-based NHEJ assay.

**Supplementary Discussion |** Additional context and interpretation that expand upon the main Discussion section of the manuscript.

**Supplementary References**

# Supplementary Tables

## Supplementary Table 1. ANOVA for Extended Data Figure 10c

| Uncorrected Fisher's LSD | Mean Diff. | 95.00% CI of diff. | Below threshold? | Summary | Individual *p* – value |
|---|---|---|---|---|---|
| Deletions >20 bp | -0.001176 | -0.04744 to 0.04509 | No | ns | 0.9573 |
| Insertions >1 bp | 0.0102 | -0.03607 to 0.05647 | No | ns | 0.6437 |
| Deletions ≤20bp | 0.007581 | -0.03869 to 0.05385 | No | ns | 0.7305 |
| Insertions 1 bp | 0.02677 | -0.01950 to 0.07303 | No | ns | 0.2351 |
| Substitutions | -0.003783 | -0.05005 to 0.04249 | No | ns | 0.8633 |
| Complex Deletions | 0.007353 | -0.03892 to 0.05362 | No | ns | 0.7383 |
| Unmodified | -0.04694 | -0.09321 to -0.00066 | Yes | * | 0.0472 |

| Test details | Mean 1 | Mean 2 | Mean Diff. | SE of Diff. | N1 | N2 | t | DF |
|---|---|---|---|---|---|---|---|---|
| Deletions >20 bp | 0.0616 | 0.06277 | -0.001176 | 0.02157 | 3 | 3 | 0.0545 | 14 |
| Insertions >1 bp | 0.01988 | 0.009684 | 0.0102 | 0.02157 | 3 | 3 | 0.4726 | 14 |
| Deletions ≤20bp | 0.4482 | 0.4406 | 0.007581 | 0.02157 | 3 | 3 | 0.3514 | 14 |
| Insertions 1 bp | 0.05208 | 0.02531 | 0.02677 | 0.02157 | 3 | 3 | 1.241 | 14 |
| Substitutions | 0.04352 | 0.0473 | -0.003783 | 0.02157 | 3 | 3 | 0.1753 | 14 |
| Complex Deletions | 0.06763 | 0.06028 | 0.007353 | 0.02157 | 3 | 3 | 0.3408 | 14 |
| Unmodified | 0.3071 | 0.354 | -0.04694 | 0.02157 | 3 | 3 | 2.176 | 14 |

## Supplementary Table 2.

| Reagent | Source | Identifier or Sequence |
|---|---|---|
| ***Antibodies & Enzymes*** | | |
| Rabbit polyclonal anti-DNA PKcs | Abcam | ab70250 |
| Rabbit polyclonal anti-Ku80/XRCC5 | Novus Biologicals | NB100-503 |
| Ku70 (D10A7) Rabbit mAb | Cell Signaling Technology | 4588S |
| Rabbit polyclonal anti-Mre11 | Novus Biologicals | NB100-142 |
| Rabbit polyclonal anti-Rad50 | Novus Biologicals | NBP2-20054 |
| Rabbit polyclonal anti-Nbs1 | Novus Biologicals | NB100-143 |
| Rabbit polyclonal anti-PARP1 | Novus Biologicals | NBP2-13732 |
| SirT6 (D8D12) Rabbit mAb | Cell Signaling Technology | 12486S |
| RPA34 (RPA2) Mouse Monoclonal Antibody [Clone ID: OTI1H10] | OriGene | TA500765 |

| | | |
|---|---|---|
| Rabbit monoclonal [EPR2877Y] to RPA32/RPA2 | Abcam | ab76420 |
| Rabbit polyclonal anti-CIRBP | Proteintech | 10209-2-AP |
| Rabbit monoclonal [EPR18783] anti- CIRP | Abcam | ab191885 |
| Goat polyclonal anti-CIRP | Abcam | ab106230 |
| Mouse monoclonal [PAb 240] anti-p53 | Abcam | ab26 |
| Rabbit polyclonal anti-p53 | Abcam | ab131442 |
| Rabbit polyclonal anti-Rb | Abcam | ab226979 |
| PTEN (D4.3) XP Rabbit mAb | Cell Signaling Technology | 9188S |
| Ras (G12V Mutant Specific) (D2H12) Rabbit mAb | Cell Signaling Technology | 14412S |
| Sv40 Large T Antigen (D1E9E) Rabbit mAb | Cell Signaling Technology | 15729S |
| Rabbit polyclonal anti-Histone H3 | Abcam | ab1791 |
| Rabbit polyclonal anti-beta actin | Abcam | ab8227 |
| Poly/Mono-ADP Ribose (E6F6A) Rabbit mAb | Cell Signaling Technology | 83732 |
| CtIP (D76F7) Rabbit mAb | Cell Signaling Technology | 9201S |
| Rabbit polyclonal anti-53BP1 | Abcam | ab172580 |
| Anti-phospho- Histone H2A.X (Ser139) Antibody, clone JBW301 | Sigma-Aldrich | 05-636 |
| Goat anti-mouse IgG H&L (HRP) | Abcam | ab6789 |
| Goat anti-rabbit IgG H&L (HRP) | Abcam | ab6721 |
| Rabbit Anti-Goat IgG H&L (HRP) | Abcam | ab6741 |
| Mouse Anti- Cyclobutane Pyrimidine Dimers (CPDs) mAb (Clone TDM-2) | Cosmo Bio | CAC-NM-DND-001 |
| Goat anti-Mouse IgG (H+L) Cross- Adsorbed Secondary Antibody, Biotin | ThermoFisher Scientific | 62-654-0 |
| Goat anti-Mouse IgG (H+L) Highly Cross-Adsorbed Secondary Antibody, Alexa Fluor™ 568 | ThermoFisher Scientific | A11031 |
| Goat Anti-Rabbit IgG H&L (Alexa Fluor® 488) | Abcam | ab150077 |
| Starbright™ Blue 520 Goat | Bio-Rad | 12005866 |

| | | |
|---|---|---|
| Anti- Mouse IgG | | |
| Starbright™ Blue 520 Goat Anti- Rabbit IgG | Bio-Rad | 12005869 |
| Streptavidin - HRP | ThermoFisher Scientific | 434323 |
| MS-grade trypsin | ThermoFisher Scientific | 90058 |
| rhCIRBP | Millipore | SRP6553 |
| rhCIRBP | Abcam | ab106903 |
| Alt-R™ S.p. Cas9 Nuclease V3 | IDT | 1081058 |
| ***Kits*** | | |
| EpiQuik Nuclear Extraction Kit | Epigentek | OP-0002-1 |
| PARP Universal Colorimetric Assay Kit | Trevigen | 4677-096-K |
| Annexin V FLUOS Staining Kit | Roche | 1988549 |
| Annexin V Apoptosis Kit [FITC] | Novus Biologicals | NBP2-29373-100Tests |
| QIAamp DNA Blood Mini Kit | Qiagen | 51104 |
| Q5 Site-Directed Mutagenesis Kit | New England Biolabs | E0554 |
| One Shot TOP10 Chemically Competent Cells | ThermoFisher Scientific | C404006 |
| Zero Blunt TOPO PCR Cloning Kit for Sequencing | ThermoFisher Scientific | 45-003-1 |
| TOPO TA Cloning Kit for Subcloning | ThermoFisher Scientific | 450641 |
| Phusion Hot Start Flex DNA Polymerase | New England Biolabs | M0535 |
| QIAprep Spin Miniprep Kit | Qiagen | 27106 |
| EndoFree Plasmid Maxi Kit | Qiagen | 12362 |
| NHDF Nucleofector® Kit | Lonza | VPD-1001 |
| P2 Primary Cell 4D-Nucleofector® X Kit L | Lonza | V4XP-2024 |
| Quick-RNA™ MiniPrep | Zymo Research | R1054 |
| RNeasy Plus Mini Kit | Qiagen | 74134 |
| Dual-Luciferase Reporter 1000 Assay System | Promega | E1980 |
| Protamine Sulfate Coated ELISA plate | Cosmo Bio | CSR-NM-MA-P002 |
| KAPA 2G Robust HotStart ReadyMix | Roche | 07961375001 |

| | | |
|---|---|---|
| S-Trap Micro Column | Protifi | C02-micro-80 |
| Wizard Genomic DNA Purification Kit | Promega | A1120 |
| QIAquick Gel Extraction Kit | Qiagen | 28706 |
| NEBNext Q5 Hot Start HiFi PCR Master Mix | New England Biolabs | M0543L |
| ***Chemicals*** | | |
| Cytochalasin B from Drechslera dematioidea | Sigma-Aldrich | C2743 |
| Methylene Blue | Sigma-Aldrich | M9140 |
| 50% Hydrogen Peroxide | Fisher Scientific | H341 |
| Antifade mounting medium with DAPI | Vector laboratories | H-1200 |
| Acridine Orange | ThermoFisher Scientific | A1301 |
| Genetic™ Selective Antibiotic (inG418 Sulfate) | ThermoFisher Scientific | 10131035 |
| Puromycin | ThermoFisher Scientific | A1113803 |
| Etoposide | Sigma-Aldrich | E1383 |
| N-Nitroso-N-ethylurea,ISOPAC | Sigma-Aldrich | N3385 |
| 6-thioguanine | Chem-Impex | 01491 |
| Nitro blue tetrazolium chloride | ThermoFisher Scientific | N6495 |
| Ethyl methanesulfonate | Sigma-Aldrich | M0880 |
| 1-Methyl-3-nitro-1-nitrosoguanidine | Selleck Chemicals | E0157 |
| T7 Exonuclease | New England Biolabs | M0263S |
| Alt-R® Cas9 Electroporation Enhancer | IDT | 1075915 |
| SYBR Gold | ThermoFisher Scientific | S11494 |
| Lipofectamine™ RNAiMAX Transfection Reagent | ThermoFisher Scientific | 13778150 |
| RNase A, DNase and protease-free (10 mg/mL) | ThermoFisher Scientific | EN0531 |
| Neocarzinostatin from Streptomyces carzinostaticus | Sigma-Aldrich | N9162-100UG |
| Bleomycin Sulfate, Streptomyces verticillus | EMD Millipore | 203401-10MG |
| VECTASHIELD PLUS Antifade Mounting Medium with DAPI | Vector Laboratories | H-2000-10 |
| ***siRNA*** | | |
| Non-target | Dharmacon | UGGUUUACAUGUCGACUAA |
| anti-bwCIRBP | Dharmacon | GACAGATCTCAGAAGTGGTGGTCGT |
| Silencer™ Select Negative Control No. 2 siRNA | ThermoFisher Scientific | 4390846 |

| | | |
|---|---|---|
| Silencer™ Select Custom anti- bwCIRBP #1 | ThermoFisher Scientific | CUACGACAGUUACGCUACA |
| Silencer™ Select Custom anti- bwCIRBP #2 | ThermoFisher Scientific | AGCAGGUCUUCUCAAAAUA |
| ***Primers & Probes*** | | |
| Pem-F | IDT | GCTAAGTGCTTAGTAAAGCAATAGACTGCAT |
| Pem-R | IDT | GGACTAGTAATTGTTTAACATGTGGGAAGTT |
| PTEN ddPCR probe | IDT | /56-FAM/ACCGCCAAG/ZEN/TCCAGAGCCAT/3IABkFQ/ |
| UCE.359 ddPCR probe | IDT | /5HEX/ATGAGACGG/ZEN/GAGACAAGTGATGCT/3IABkFQ/ |
| UCE.359-F | IDT | ATCTGAGACTTGTGACAT |
| UCE.359-R | IDT | GTGTTAATTGGTAATGACTATT |
| RB1 KO up-F | IDT | TCGGGAAGAGACAGGTTCAG |
| RB1 KO up-R | IDT | TCGCTCCCGAACCCAAA |
| RB1 KO down 1-F | IDT | ACTAAAAGGTCTGAGTGAGTGC |
| RB1 KO down 1-R | IDT | CTCATATGAGAAGCCCAGAAGG |
| RB1 KO down 2-F | IDT | ACTAAAAGGTCTGAGTGAGTGC |
| RB1 KO down 2-R | IDT | CTTTCGAAGCAGAACTCCAAAC |
| TP53 KO up-F | IDT | GCAGAAATAGGTAGACACTGAGGAA |
| TP53 KO up-R | IDT | ACGGGAGAAACGAGAGTCAGAA |
| TP53 KO down 1- F | IDT | CTTCCTGTGTTGGAAAGCCATG |
| TP53 KO down 1- R | IDT | CACCAAGCAGAGGTTTAAGCAC |
| TP53 KO down 2- F | IDT | CTTCCTGTGTTGGAAAGCCATG |
| TP53 KO down 2- R | IDT | CTGCCCCTTCTTAGACTTCAGG |
| PTEN KO up-F | IDT | CAGTCGCTGCAACCATCCA |
| PTEN KO up-R | IDT | ATCCGACCAGGGTTAAATGTCATAG |
| PTEN KO down 1- F | IDT | AAGAGGGTCATTTAAAAGGCCC |
| PTEN KO down 1- R | IDT | TCTGACACAATGTCCTATTGCC |
| PTEN KO down 2- F | IDT | TAGGGCGAATGGAATCCTAAAC |
| PTEN KO down 2- R | IDT | TCTGACACAATGTCCTATTGCC |
| PTEN fidelity-F | IDT | TGGCTGCTGAGGAGAAGC |
| PTEN fidelity-R | IDT | GCATCCGTCTACTCCCACG |
| PTEN fidelity-R (cow SNP) | IDT | GCATCCGTCTATTCCCACG |
| PTEN ddPCR-F | IDT | TTCTGCCATCTCTCTCC |
| PTEN ddPCR-R | IDT | CAGGTCAAGTCTAAGTCG |
| Lego-iC2-hCIRBP- F | IDT | CCGCGAATTCGCCACCATGGCATCAGATGAAGGCAAAC |
| Lego-iC2-hCIRBP- R | IDT | CCGCGCGGCCGCTTACTCGTTGTGTGTAGCGTAACTGTCATAACTGTCTC |
| Lego-iC2- bwCIRBP-F | IDT | CCGCGAATTCGCCACCATGGCATCAGATGAGGGC |
| Lego-iC2- bwCIRBP-R | IDT | CCGCGCGGCCGCTTACTCGTTGTGTGTAGCGTAACTGTCGTAGC |
| ***CRISPR Guide RNAs*** | | |

| | | |
|---|---|---|
| Alt-R® CRISPR-Cas9 tracrRNA | IDT | 1072533 |
| Alt-R® CRISPR-Cas9 tracrRNA, ATTO™ 550 | IDT | 1075928 |
| RB1 KO crRNA 1 | IDT | GCTGCTCTACGGGGGGTTTT |
| RB1 KO crRNA 2 | IDT | GGCTGCTCTACGGGGGGTTT |
| RB1 KO crRNA 3 | IDT | AGACACCAGCTGATACTACG |
| TP53 KO crRNA 1 | IDT | GTCACAGGCAGAACTCGGCG |
| TP53 KO crRNA 2 | IDT | CGTGGAGCCCCCTCTGAGTC |
| TP53 KO crRNA 3 | IDT | AAATAGGGGAGTGATAACCG |
| PTEN KO crRNA 1 | IDT | GCTAACGATCTCTTTGATGA |
| PTEN KO crRNA 2 | IDT | AGATCGTTAGCAGAAACAAA |
| PTEN KO crRNA 3 | IDT | ATTCTCTGGATCAGAGTCAG |
| PTEN fidelity crRNA | IDT | GCTAACGATCTCTTTGATGA |
| ***Plasmids*** | | |
| pPB-SV40 large T (LT) | Tian, X. et al. (2018) 1 | |
| pPB-LTK1 | Tian, X. et al. (2018)1 | |
| pPB-LTΔ434 – 444 | Tian, X. et al. (2018)1 | |
| pPB- SV40 small T (ST) + LT | Tian, X. et al. (2018)1 | |
| pPB-H-Ras V12 | Tian, X. et al. (2018)1 | |
| pPB-hTERT | Tian, X. et al. (2018)1 | |
| Super PiggyBac Transposase Expression Vector | System Biosciences | PB210PA-1 |
| pRP[Exp]-Neo- CMV-hCIRBP | VectorBuilder | VB210330-1269gmt |
| pRP[Exp]-Neo- CMV-bwCIRBP | VectorBuilder | VB210330-1268bpc |
| pRP[Exp]-Neo-CMV-bwCIRBP- RGG 9R/A | VectorBuilder | VB220320-1032yqx |
| pRP[Exp]-Neo- CMV-Puro | VectorBuilder | VB220318-1212uym |
| pCMV-Luc | Tian, X. et al. (2019)2 | |
| pCMV-RL | Promega | E2261 |
| NHEJ reporter construct | Mao, Z. et al. (2011)3 | |
| HR reporter construct | Mao, Z. et al. (2011)3 | |
| pCMV-ISce1 | Mao, Z. et al. (2011)3 | |
| pDsRed | Mao, Z. et al. (2011)3 | |
| LeGO-iC2-Luciferase | This manuscript | |
| LeGO-iC2-hCIRBP | This manuscript | |
| LeGO-iC2- bwCIRBP | This manuscript | |
| pp53-TA-Luc | Clontech (Takara) | 631914 |
| pE2F-TA-Luc | Clontech (Takara) | 631914 |
| pRb-TA-Luc | Clontech (Takara) | 631914 |
| Lego-iC2 | Addgene | 27345 |
| pVSV-G | Addgene | 138479 |

| | | |
|---|---|---|
| psPAX2 | Addgene | 12260 |
| pmaxGFP | Lonza | VPD-1001 |
| ***Cell Lines*** | | |
| 14B8SF | Isolated by authors | Primary dermal fibroblasts isolated from adult female bowhead whale 14B8 [4] |
| 14B10SF | Isolated by authors | Primary dermal fibroblasts isolated from adult male bowhead whale 14B10 [4] |
| 14B11SF | Isolated by authors | Primary dermal fibroblasts isolated from adult male bowhead whale 14B11 [4] |
| 18B2SF | Isolated by authors | Primary dermal fibroblasts isolated from adult female bowhead whale 18B2 [5] |
| 18B9SF | Isolated by authors | Primary dermal fibroblasts isolated from adult male bowhead whale 18B9 [5] |
| 18B12SF | Isolated by authors | Primary dermal fibroblasts isolated from adult female bowhead whale 18B12 [5] |
| NHDF1 | ATCC | PCS-201-012, Lot 64540954, normal adult male human primary dermal fibroblasts |
| NHDF2 | ATCC | PCS-201-012, Lot 63792061, normal adult male human primary dermal fibroblasts |
| NHDF3 | ATCC | PCS-201-012, normal adult male human primary dermal fibroblasts |
| YAHSF | Isolated by authors | Normal adult male human primary dermal fibroblasts |
| HCA2 | Isolated by authors | Normal neonatal male foreskin primary dermal fibroblasts |
| BT1SF | Isolated by authors | Primary dermal fibroblasts isolated from adult *Bos taurus.* |
| BT2SF | Isolated by authors | Primary dermal fibroblasts isolated from adult *Bos taurus.* |
| BT3SF | Isolated by authors | Primary dermal fibroblasts isolated from adult male *Bos taurus* |
| BT4SF | Isolated by authors | Primary dermal fibroblasts isolated from adult female *Bos taurus* |
| BT5SF | Isolated by authors | Primary dermal fibroblasts isolated from adult female *Bos taurus* |
| WTMSF9 | Isolated by authors | Primary dermal fibroblasts isolated from wild-caught adult male mouse *Mus musculus* |
| WTMSF10 | Isolated by authors | Primary dermal fibroblasts isolated from wild-caught adult male mouse *Mus musculus* |
| WTMSF11 | Isolated by authors | Primary dermal fibroblasts isolated from wild-caught adult female mouse *Mus musculus* |
| WTMSF15 | Isolated by authors | Primary dermal fibroblasts isolated from wild-caught adult female mouse *Mus musculus* |
| MSF10 | Isolated by authors | Primary dermal fibroblasts isolated from C57BL6/J adult mouse *Mus musculus* |
| Hippopotamus primary | San Diego Zoo Wildlife Alliance | Primary dermal fibroblasts isolated from |

| | | |
|---|---|---|
| fibroblasts | | Hippopotamus |
| Common dolphin fibroblasts | San Diego Zoo Wildlife Alliance | Primary dermal fibroblasts isolated from Common dolphin |
| Humpback whale primary fibroblasts | San Diego Zoo Wildlife Alliance | Primary dermal fibroblasts isolated from Humpback whale |
| Bottlenose dolphin primary fibroblasts | Isolated by authors | Primary dermal fibroblasts isolated from bottlenose dolphin collected by Georgia Aquarium through Tara Harrison (Exotic Species Cancer Research Alliance) |
| California sea lion primary fibroblasts | Isolated by authors | Primary dermal fibroblasts from California sea lion collected by the Marine Mammal Care Center Los Angeles under Institutional Animal Care and Use Committee oversight and National Marine Fisheries Service permit number 21636. |
| Lenti-X 293T | Clontech (Takara) | 632180 |

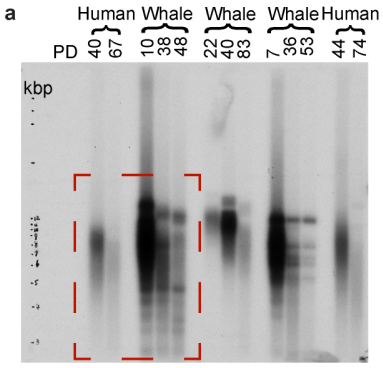


Used in Figure 1c

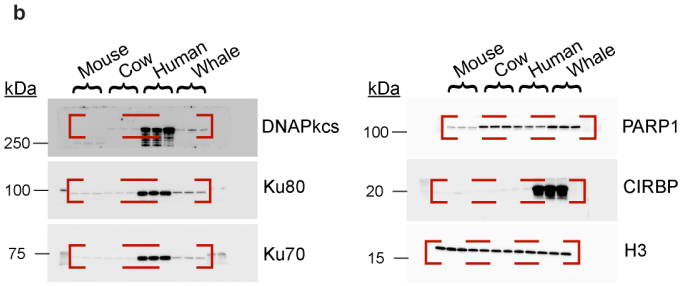


Used in Figure 4a

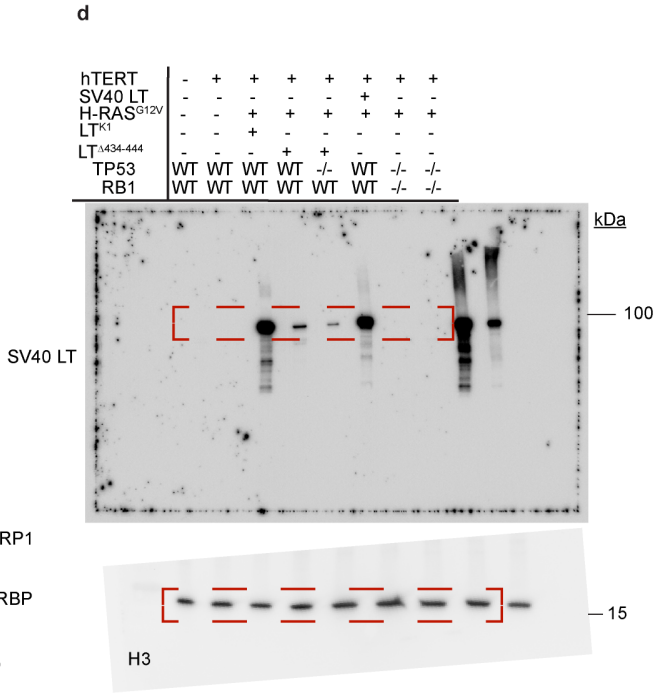


Used in Extended data Figure 1d

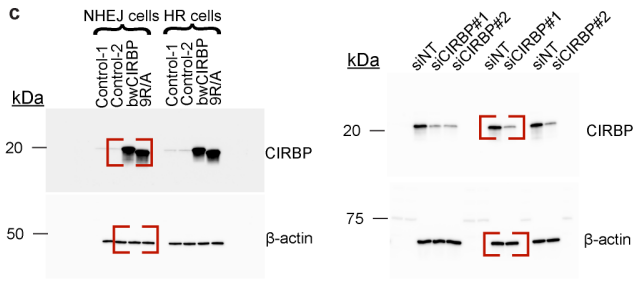


Used in Figure 4d

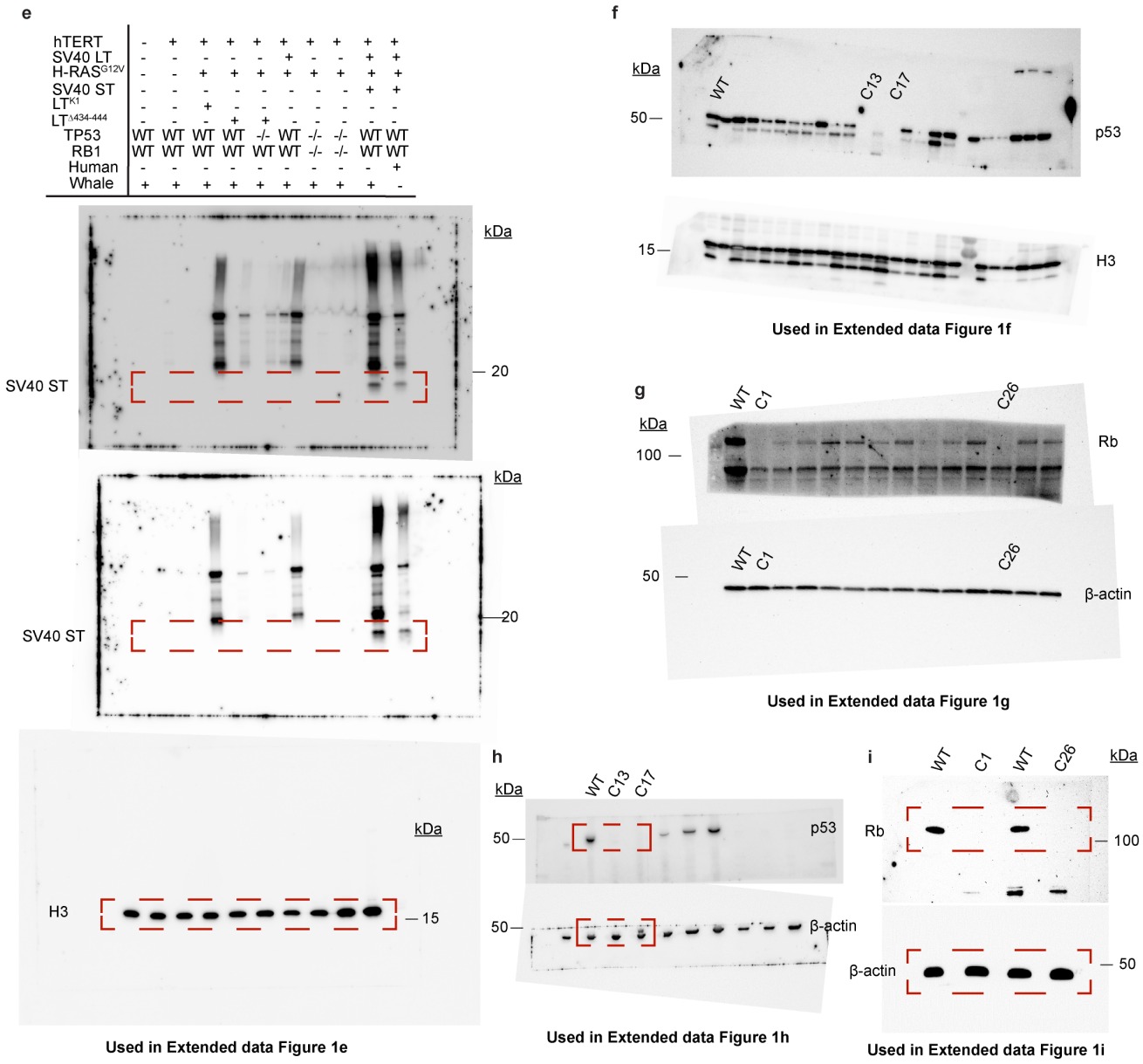


**Supplementary Figure 1 |** Uncropped gels and Western blots from Main and Extended Data Figures.

**a** **TP53 upstream**

TP53$^{-/-}$ clone 13

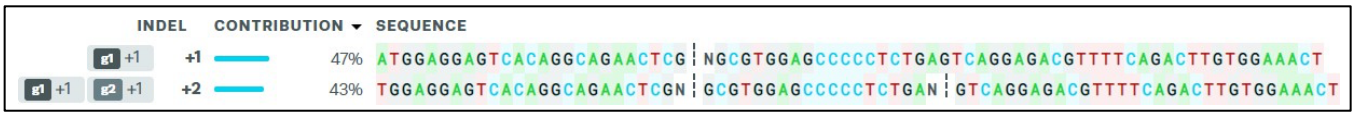


TP53$^{-/-}$ clone 17

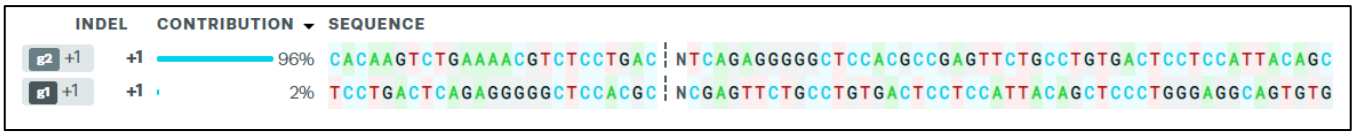


TP53$^{-/-}$RB$^{-/-}$ clone 1

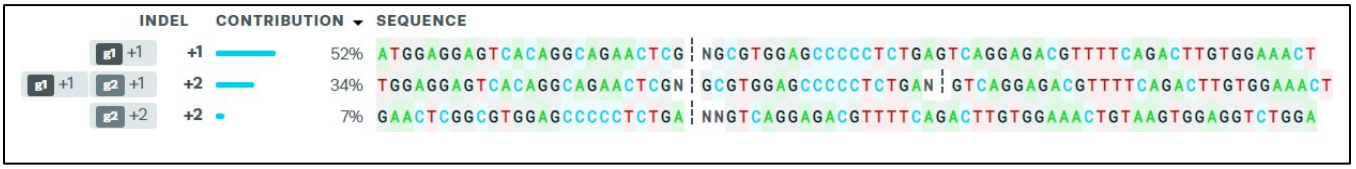


TP53$^{-/-}$Rb$^{-/-}$ clone 26


**b** **TP53 downstream**

TP53$^{-/-}$ clone 13


TP53$^{-/-}$ clone 17


TP53$^{-/-}$RB$^{-/-}$ clone 1


TP53$^{-/-}$Rb$^{-/-}$ clone 26


**Supplementary Figure 2 | Synthego ICE analysis of Sanger sequencing data from TP53-edited clones. (a)** Synthego ICE deconvolution results from Sanger sequencing traces of PCR products amplified from the upstream TP53 CRISPR target site in the indicated cell lines. Alleles with estimated frequencies near 100% are considered

homozygous, while two alleles with approximately 50% frequency each indicate heterozygosity. Predicted alleles with frequencies below 10% are attributed to background noise in the Sanger traces. **(b)** ICE analysis results for PCR amplicons from the downstream TP53 CRISPR target site in the same cell lines.

**a** **RB1 upstream**

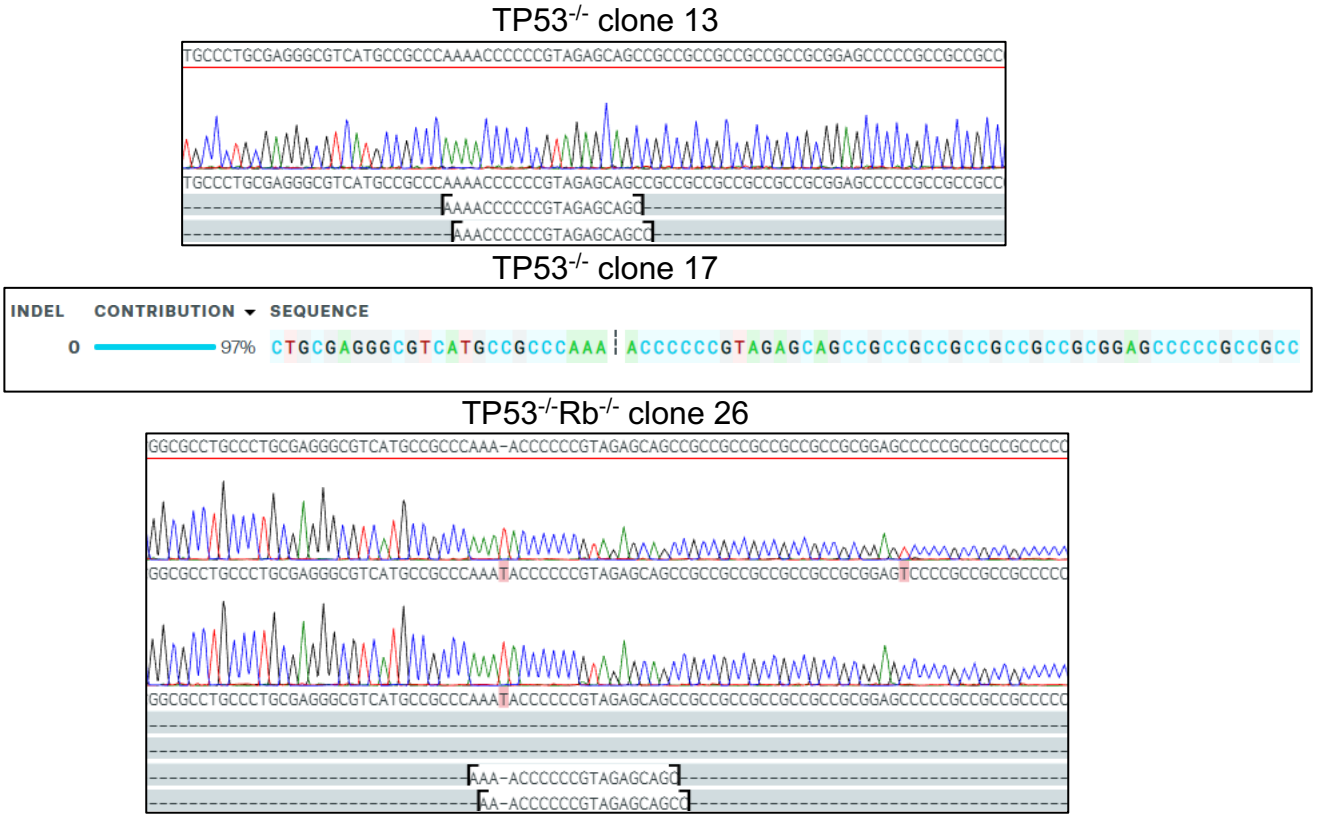


**b** **RB1 downstream**

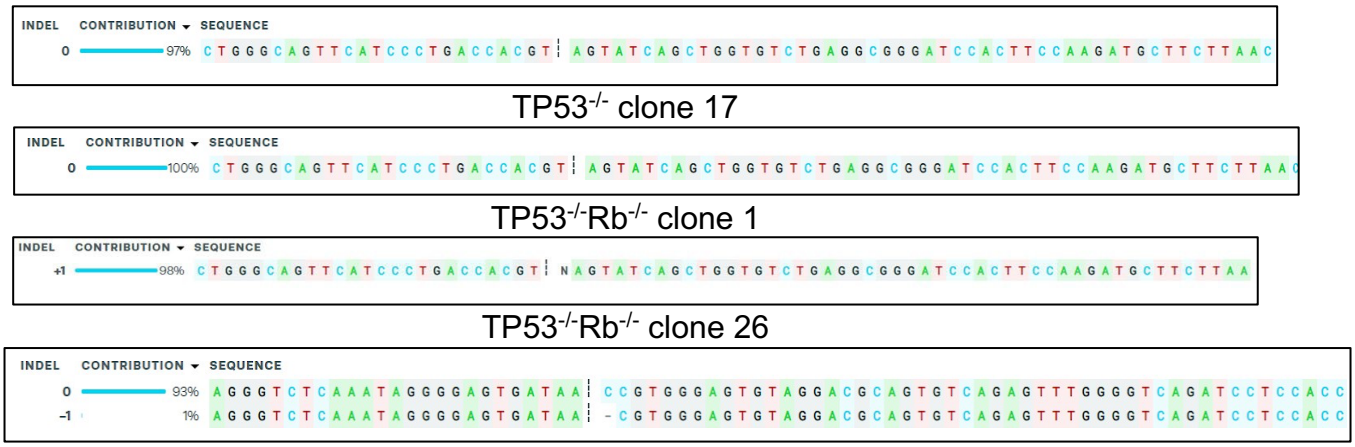


**Supplementary Figure 3 | Synthego ICE analysis and TOPO sequencing of RB1-edited clones. (a)** Synthego ICE deconvolution results from Sanger sequencing traces of PCR products amplified from the upstream RB1 CRISPR target site in the indicated cell lines. Alleles with estimated frequencies near 100% are considered homozygous,

while two alleles with approximately 50% frequency each indicate heterozygosity. Predicted alleles with frequencies below 10% are considered likely to reflect background noise in the Sanger traces. For samples that failed ICE analysis, individual alleles were sequenced using TOPO cloning followed by Sanger sequencing of bacterial colonies. Resulting sequences are aligned to the RB1 reference, with guide RNA sequences shown below each alignment (generated using Benchling). **(b)** ICE deconvolution results from PCR amplicons corresponding to the downstream RB1 CRISPR target site in the same cell lines.

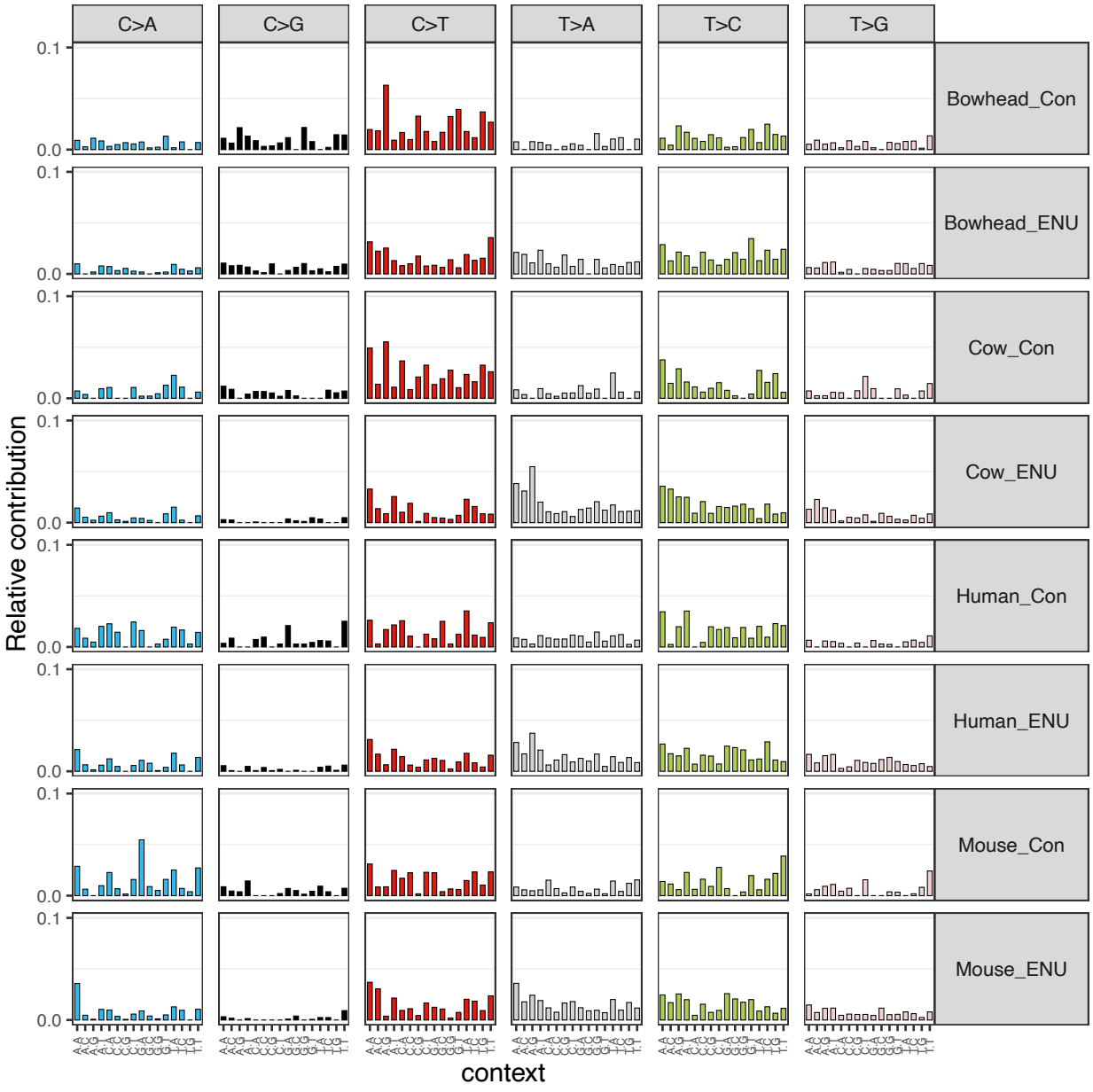


**Supplementary Figure 4 | Mutational spectra for all sampled groups in the study.** Samples are grouped by species and treatment status. Mutation counts were normalized by the ratio of trinucleotide frequencies between human and the other species. “Con” indicates untreated control groups. The x-axis (“context”) shows mutational profiles according to the conventional 96 mutation-type classification used in COSMIC. This classification is based on six base substitution types (shown above the plot) and the immediate 5′ and 3′ nucleotide context (sorted by A, C, G, and T).


**Supplementary Figure 5 | Alignment of PTEN target sequences used in cross-species DSB repair fidelity assays.** Alignment of next-generation sequencing (NGS) amplicon sequences for each species, alongside the human PTEN exon 1 reference and the guide RNA target site, as used in comparative CRISPR-based DSB repair fidelity experiments. The amplicon and primer pair were designed to accommodate paired-end sequencing, ensure conservation of internal sequence and primer binding sites across species, and allow detection of large deletions. Preliminary Sanger sequencing with a longer amplicon revealed that such deletions frequently occur upstream of the guide RNA site. Mismatches relative to the consensus sequence are highlighted in red. Alignments were generated using Clustal Omega in Benchling.

**a**

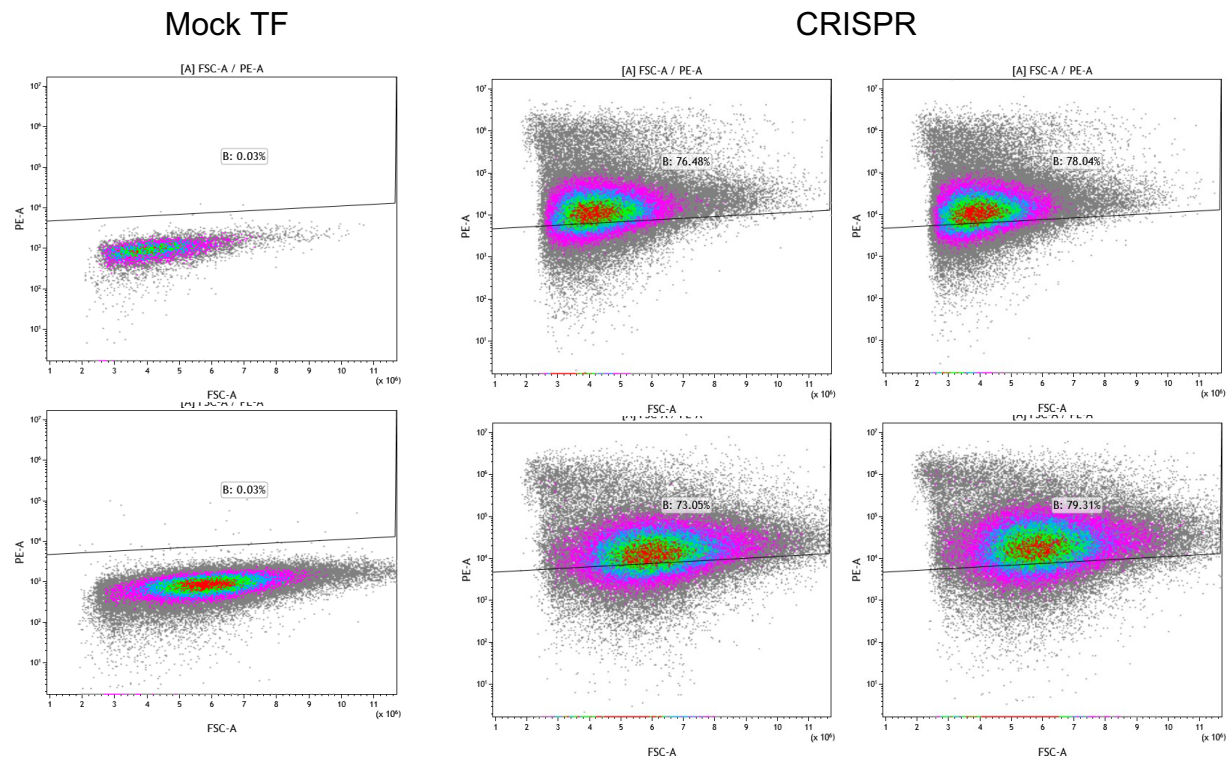


**b**

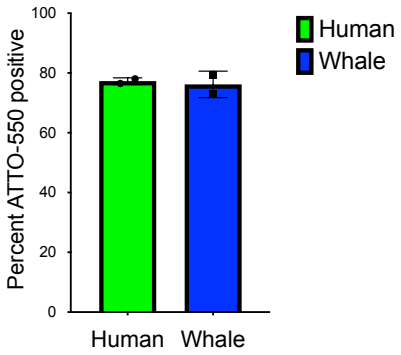


**Supplementary Figure 6 | Transfection efficiency of CRISPR RNPs labeled with ATTO 550. (a)** Flow cytometry analysis of ATTO 550-positive cells immediately (0 h) after transfection of CRISPR ribonucleoprotein (RNP) complexes into primary fibroblasts from human and bowhead whale. The ATTO 550-positive gate was set using mock-transfected controls. Plots in each row show results by species for mock transfection and replicate ATTO 550-labeled RNP transfections. **(b)** Quantification of average ATTO 550-positive cell percentages for each species.

**Mock transfection** **ISce-I/DsRed transfection**

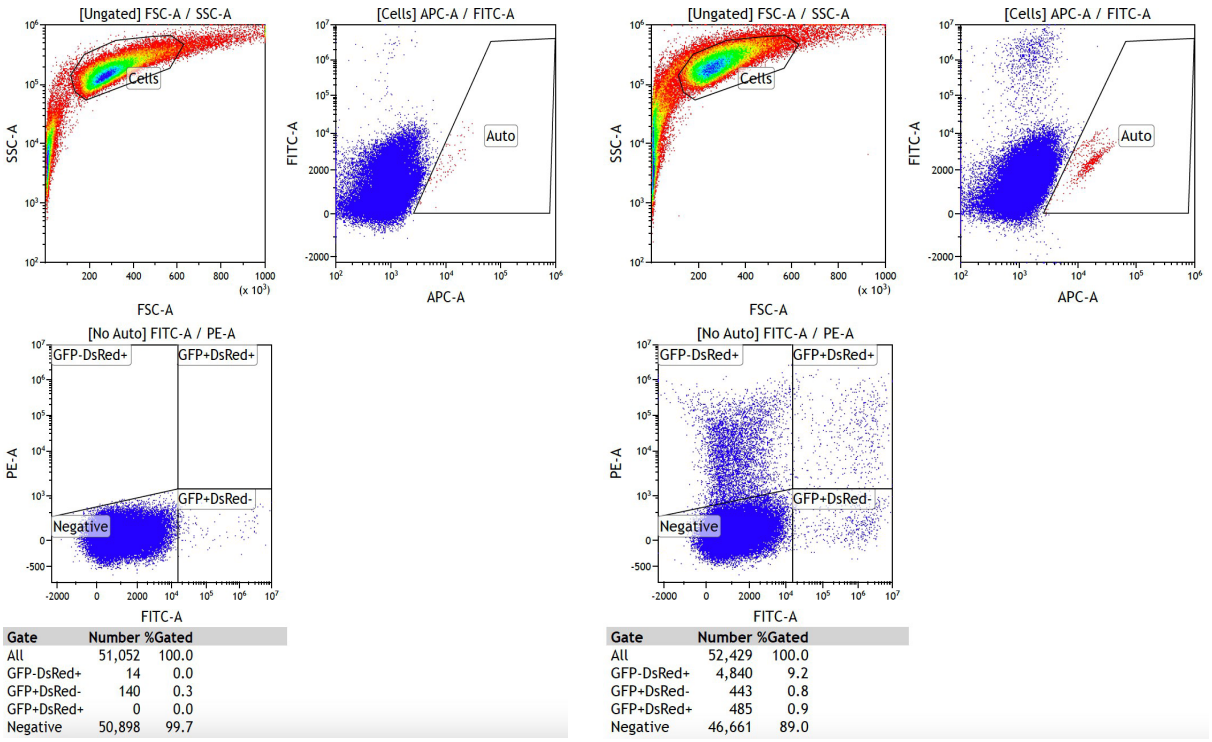


| Gate | Number | %Gated |
|---|---|---|
| All | 51,052 | 100.0 |
| GFP-DsRed+ | 14 | 0.0 |
| GFP+DsRed- | 140 | 0.3 |
| GFP+DsRed+ | 0 | 0.0 |
| Negative | 50,898 | 99.7 |

| Gate | Number | %Gated |
|---|---|---|
| All | 52,429 | 100.0 |
| GFP-DsRed+ | 4,840 | 9.2 |
| GFP+DsRed- | 443 | 0.8 |
| GFP+DsRed+ | 485 | 0.9 |
| Negative | 46,661 | 89.0 |

**Supplementary Figure 7 | Gating strategy for flow cytometry-based NHEJ assay.** Mock-transfected cells were used to define positive and negative gates, which were then applied uniformly to all samples within each experiment. The live, singlet cell population was gated using forward scatter (FSC) and side scatter (SSC) parameters, with exclusion of cellular debris. Autofluorescent cells were excluded based on APC channel fluorescence. NHEJ frequency was calculated by determining the proportions of $GFP^+$ and $DsRed^+$ cells in the FITC–PE plot. Fluorescence compensation was performed using Kaluza software.

## Supplementary Discussion

**Bowhead whale is not impervious to senescence and apoptosis.** While we found bowhead whale cells to have enhanced DNA repair capacity, they still underwent senescence and apoptosis when subjected to DNA damage. The doses of gamma-irradiation we used for induction of stress-induced premature senescence were too high to be overcome by DNA repair. At such saturating doses of irradiation normal fibroblasts induce cell cycle checkpoints by activating p53-p21/p16 axis. Thus, CIRBP does abolishes tumor-suppressive checkpoints or globally suppresses senescence or apoptosis.

**CIRBP role in DSB repair.** Our data demonstrate that CIRBP stimulates both major DSB repair pathways, NHEJ and HR, and in a purified system, promotes DNA ligation, protects DNA ends from exonuclease-mediated degradation, and enhances DNA binding of the core NHEJ factor Ku70/80. Our data and prior work indicate that CIRBP acts at an early, pathway-agnostic step by stabilizing damaged chromatin and promoting DSB signaling rather than enforcing the NHEJ/HR decision. In such an upstream role, a single factor can facilitate both outcomes: transient protection of DNA ends, and enhanced recruitment/activation of DDR factors improve repair competence generally. SIRT6 is another factor that acts upstream to promote both NHEJ and HR[3].

Consistent with the role of CIRBP in both NHEJ and HR, Chen et al.[6], showed that CIRBP accumulates at breaks in a PARP1-dependent manner, and CIRBP depletion impairs both HR and NHEJ while reducing MRN/ATM chromatin association and ATM-substrate phosphorylation - hallmarks of an upstream facilitator rather than a pathway-specific effector.

A potential mechanism by which CIRBP promotes end-joining and/or protects DNA ends from excessive degradation *in vivo* may involve its recruitment to damaged DNA, a process enhanced by PAR and RNA. Within the repair complex, CIRBP may promote DNA ligation through direct interaction with DNA and DNA repair proteins. Another possible mechanism is through liquid-liquid phase separation (LLPS). CIRBP has been shown to undergo LLPS *in vitro*[7]. Recent studies suggest that RNA-binding proteins can promote LLPS at DNA DSB sites, which may help concentrate repair factors and stabilize broken DNA ends. For example, the FUS RNA-binding protein was found to maintain

genomic stability and promote formation of droplet-like compartments in response to DNA damage[8]. Furthermore, it has been shown that long non-coding RNAs synthesized at DSBs are necessary to drive molecular crowding of 53BP1 into foci that exhibit LLPS condensate properties[9]. CIBRP may form condensates around the broken DNA protecting the ends from degradation and facilitating recruitment of DNA repair factors. While overexpression of DNA repair enzymes may be detrimental, the potential role of CIRBP in forming a protective condensate around a DSB, is consistent with more abundant CIRBP providing greater benefit.

In the bowhead whale cells, CIRBP recruitment to damaged chromatin was RNA-dependent. (**Extended Data Fig. 11a–c**), whereas recombinant CIRBP bound DNA substrates directly in vitro (**Extended Data Fig. 11f, g**). A likely explanation for this discrepancy is that RNA binding likely facilitates recruitment of CIRBP to damaged chromatin, whereas in the purified system, CIRBP is premixed with DNA ends and NHEJ factors, thereby bypassing the recruitment step.

**Improved MMR in the bowhead whale.** In addition to DSB repair, we found the bowhead whale to possess very accurate MMR. While the exact mechanisms leading to the enhanced MMR are beyond the scope of this study, we observed multiple genes in the MMR pathway to be upregulated in the bowhead whale (**Extended Data Fig. 8**).

Other factors likely to be involved in improved DSB repair in the bowhead whale. CIRBP stood out as the most highly elevated DNA repair factor in the bowhead whale. However, many other DSB repair proteins were elevated in cells from this long-lived species, including PARP1, RPA2, CtIP, and others. Working in concert, all these proteins are likely to contribute to enhanced genome stability in the bowhead whale. Of all DNA repair pathways, DNA DSB repair shows the strongest link to longevity, with mutations in DNA DSB repair genes resulting in premature aging syndromes[10]. Furthermore, a study of 20 rodent species with diverse lifespan found a strong correlation between longevity and more efficient DSB repair, but not NER[2]. Consistently, expression of DNA DSB repair genes was found to be positively correlated with longevity in a transcriptomic study of 26 mammalian species[11]. In addition to DSB repair, we found the mismatch repair pathway to be enhanced in the bowhead whale. This was accompanied by increased expression of several mismatch repair genes. Future studies will be focused on defining the

mechanisms responsible for enhanced mismatch repair in the bowhead whale.

Prior work has identified positive selection in cancer-related genes such as *CXRC2, ADAMTS8, and ANXA1* in cetaceans, as well as cetacean-specific evolutionary changes to multiple FGF genes[12,13]. Expansion of the eukaryotic initiation factor 2, polyadenylate binding protein, and 60S ribosomal L10 gene families have also been identified in the genome of the bowhead whale, potentially implying substantial alterations to translational regulation[14]. An additional anti-cancer mechanism was recently reported for the bowhead whale in the form of a *CDKN2C* checkpoint gene duplication[15]. It has further been suggested that the low body temperature and low metabolic rate of the bowhead whale may also contribute to its extended lifespan[16]. Indeed, it is likely that numerous individual factors combine to modify cancer risk and produce the longest mammalian lifespan.

**Evolution of CIRBP and accurate DNA repair in baleen whales.** CIRBP is highly abundant in the bowhead whale compared to most other mammals. We speculate that baleen whales evolved this high CIRBP abundance as an adaptation to life in cold water, and that CIRBP was subsequently co-opted to facilitate genome maintenance.

One potential drawback of a highly accurate DNA repair system could be a reduction in genetic variation and thus a slower rate of evolution of traits. However, species living in safe and stable environments have less evolutionary pressure to rapidly evolve new adaptations. A genome analysis of long-lived rockfishes living in deep ocean revealed positive selection in DNA repair pathways[17]. Interestingly, a recent analysis of germline mutations in baleen whales based on analysis of pedigrees concluded that germline mutation frequencies are similar to those in primates, in contrast to prior studies finding reduced germline mutation rates in whales[18]. Thus, it appears that germline and somatic mutation rates are not inherently linked and could respond to selection independently[19].

Why would improved DNA repair have evolved in the bowhead whale, as opposed to the often-proposed solution to Peto's Paradox of increased tumor suppressor copy number and elevated apoptotic response? One possible explanation is that tumor suppressors, apoptosis, and senescence all appear to pose costs to the organism and force tradeoffs between cancer and cell depletion leading to age-related degeneration.

Simply shifting the balance from apoptosis/senescence to survival and repair could be detrimental if not also coupled with increased fidelity, as evidenced by the frequent upregulation of DNA repair pathways in cancer cells[20]. However, evolutionary innovations in DNA repair that couple high efficiency with high fidelity could promote long-term tissue function and maintenance at both the cellular and genomic levels. Maintenance of genome stability would reduce cancer risk and, as suggested by a rapidly growing body of evidence implicating age-related somatic mosaicism as a ubiquitous feature and functional driver of aging[21–25], additionally protecting against other aspects of age-related decline. Thus, the lower accuracy and efficiency of DNA repair observed in mammals with shorter lifespans may simply reflect the absence of sufficient selective pressure[88]. Indeed, there is little selective advantage of DNA repair capacity to last far beyond reproductive age.

**Therapeutic hypothermia.** The therapeutic benefits of cold exposure have been recognized for centuries, with practices such as brief cold-water immersion believed to promote health and resilience in Nordic cultures. In modern medicine, whole-body cryotherapy is widely employed in sports medicine to reduce inflammation and enhance recovery following exercise or injury[26]. Although the molecular mechanisms underlying the effects of cryotherapy remain incompletely understood, we speculate that increased expression of the cold-inducible RNA-binding protein CIRBP may contribute to these benefits by promoting DNA repair.

Consistent with this idea, hypothermia-induced upregulation of human CIRBP significantly increased non-homologous end joining (NHEJ) frequency (**Extended Data Fig. 10e**).

While cold showers result in mild and transient reductions in body temperature, therapeutic hypothermia—the artificial reduction of core body temperature—is routinely applied in clinical settings such as cardiac or neurosurgical procedures[27]. Notably, recovery following therapeutic hypothermia is impaired in CIRBP-knockout (CIRBP-KO) rats but improved in animals with transgenic CIRBP overexpression[28]. Similar protective effects of CIRBP during hypothermia have been reported in the brain[29], kidney[30], intestine[31], and cold-preserved hearts[32].

Given that bowhead whale CIRBP (bwCIRBP) confers substantially higher protein

expression, its properties may eventually inform strategies to enhance tissue resilience under stress, for example during surgery or organ preservation. However, such applications remain speculative and will require extensive validation in relevant models.

**Supplementary References**


1. Tian, X. *et al.* Evolution of telomere maintenance and tumour suppressor mechanisms across mammals. *Philosophical Transactions of the Royal Society B: Biological Sciences* **373**, (2018).
2. Tian, X. *et al.* SIRT6 Is Responsible for More Efficient DNA Double-Strand Break Repair in Long-Lived Species. *Cell* **177**, 622-638.e22 (2019).
3. Mao, Z. *et al.* SIRT6 promotes DNA repair under stress by activating PARP1. *Science (1979)* **332**, 1443–1446 (2011).
4. Suydam, R. *et al. Subsistence Harvest of Bowhead Whales (Balaena Mysticetus) by Alaskan Eskimos during 2014*. http://www.north-slope.org/assets/images/uploads/SC-66a-BRG06.suydam.pdf.
5. Suydam, R. *et al.* Subsistence harvest of bowhead whales (Balaena mysticetus) by Alaskan Natives during 2018.
6. Chen, J. K., Lin, W. L., Chen, Z. & Liu, H. wen. PARP-1-dependent recruitment of cold-inducible RNA-binding protein promotes double-strand break repair and genome stability. *Proc Natl Acad Sci U S A* **115**, E1759–E1768 (2018).
7. Lenard, A. J. *et al.* Phosphorylation Regulates CIRBP Arginine Methylation, Transportin-1 Binding and Liquid-Liquid Phase Separation. *Front Mol Biosci* **8**, (2021).
8. Reber, S. *et al.* The phase separation-dependent FUS interactome reveals nuclear and cytoplasmic function of liquid-liquid phase separation. *Nucleic Acids Res* **49**, 7713–7731 (2021).
9. Pessina, F. *et al.* Functional transcription promoters at DNA double-strand breaks mediate RNA-driven phase separation of damage-response factors. *Nat Cell Biol* **21**, 1286–1299 (2019).
10. Gorbunova, V. & Seluanov, A. DNA double strand break repair, aging and the chromatin connection. *Mutation Research/Fundamental and Molecular Mechanisms of Mutagenesis* **788**, 2–6 (2016).
11. Lu, J. Y. *et al.* Comparative transcriptomics reveals circadian and pluripotency networks as two pillars of longevity regulation. *Cell Metab* **34**, 836-856.e5 (2022).
12. Nam, K. *et al.* Analysis of the FGF gene family provides insights into aquatic adaptation in cetaceans. *Scientific Reports 2017 7:1* **7**, 1–13 (2017).
13. Tejada-Martinez, D., De Magalhães, J. P. & Opazo, J. C. Positive selection and gene duplications in tumour suppressor genes reveal clues about how cetaceans resist cancer. *Proceedings of the Royal Society B* **288**, (2021).
14. Doherty, A. & de Magalhães, J. P. Has gene duplication impacted the evolution of Eutherian longevity? *Aging Cell* **15**, 978 (2016).
15. Vazquez, J. M., Kraft, M. & Lynch, V. J. A CDKN2C retroduplication in Bowhead whales is associated with the evolution of extremely long lifespans and alerted cell cycle dynamics. *bioRxiv* 2022.09.07.506958 (2022)

doi:10.1101/2022.09.07.506958.
16. Keil, G., Cummings, E. & de Magalhães, J. P. Being cool: how body temperature influences ageing and longevity. *Biogerontology* **16**, 383 (2015).
17. Kolora, S. R. R. *et al.* Origins and evolution of extreme life span in Pacific Ocean rockfishes. *Science* **374**, 842–847 (2021).
18. Suárez-Menéndez, M. *et al.* Wild pedigrees inform mutation rates and historic abundance in baleen whales. *Science* **381**, 990–995 (2023).
19. Lynch, M. Evolution of the mutation rate. *Trends in Genetics* **26**, 345–352 (2010).
20. Yoshioka, K. I., Kusumoto-Matsuo, R., Matsuno, Y. & Ishiai, M. Genomic Instability and Cancer Risk Associated with Erroneous DNA Repair. *International Journal of Molecular Sciences 2021, Vol. 22, Page 12254* **22**, 12254 (2021).
21. Yokoyama, A. *et al.* Age-related remodelling of oesophageal epithelia by mutated cancer drivers. *Nature* **565**, 312–317 (2019).
22. Martincorena, I. *et al.* Somatic mutant clones colonize the human esophagus with age. *Science* **362**, 911–917 (2018).
23. Jaiswal, S. *et al.* Age-related clonal hematopoiesis associated with adverse outcomes. *N Engl J Med* **371**, 2488–2498 (2014).
24. Martincorena, I. *et al.* High burden and pervasive positive selection of somatic mutations in normal human skin. *Science (1979)* **348**, 880–886 (2015).
25. Mitchell, E. *et al.* Clonal dynamics of haematopoiesis across the human lifespan. *Nature 2022 606:7913* **606**, 343–350 (2022).
26. Lombardi, G., Ziemann, E. & Banfi, G. Whole-Body Cryotherapy in Athletes: From Therapy to Stimulation. An Updated Review of the Literature. *Front Physiol* **8**, 258 (2017).
27. Gocoł, R. *et al.* The Role of Deep Hypothermia in Cardiac Surgery. *Int J Environ Res Public Health* **18**, (2021).
28. Liu, Y. *et al.* Chronic hypoxia–induced Cirbp hypermethylation attenuates hypothermic cardioprotection via down-regulation of ubiquinone biosynthesis. *Sci Transl Med* **11**, (2019).
29. Wu, L. *et al.* Therapeutic Hypothermia Enhances Cold-Inducible RNA-Binding Protein Expression and Inhibits Mitochondrial Apoptosis in a Rat Model of Cardiac Arrest. *Mol Neurobiol* **54**, 2697–2705 (2017).
30. Yu, L., Gu, T., Liu, Y., Jiang, X. & Shi, E. Cold-inducible ribonucleic acid-binding protein attenuates acute kidney injuries after deep hypothermic circulatory arrest in rats. *Interact Cardiovasc Thorac Surg* **26**, 124–130 (2018).
31. Li, Y. *et al.* Cold-inducible RNA-binding protein maintains intestinal barrier during deep hypothermic circulatory arrest. *Interact Cardiovasc Thorac Surg* **29**, 583–591 (2019).
32. Pan, H. Z. *et al.* Cold-inducible RNA binding protein agonist enhances the cardioprotective effect of UW solution during extended heart preservation. *Artif Organs* **44**, E406–E418 (2020).